Proceedings of the 2021 IEEE
International Conference on Robotics and Biomimetics
December 27-31, 2021, Sanya, China

2021 IEEE International Conference on Robotics and Biomimetics (ROBIO) | 978-1-6654-0535-5/21/$31.00 ©2021 IEEE | DOI: 10.1109/ROBIO54168.2021.9739559

Design and Modeling of a Reloadable Coil-Delivery Instrument for Aneurysm Embolization

Chuanxiang Zhu, Yifan Wang, Yue Ding, Xiang Wang and Kai Xu, *IEEE Member*

***Abstract*—Aneurysm, which weakens blood vessels and is possibly lethal, can be treated by coil embolization. The detachable coil is a preferred type of embolic agent for aneurysm treatment because it offers good coil control and ease of use. On the other hand, detachable coils can be more affordable, if the coil-delivery instrument can be reusable. To achieve the reusability of a coil-delivery instrument while keeping the operation simple, this paper presents the development and experimental characterizations of a reloadable coil-delivery instrument for the deployment of detachable coils. The instrument has a distal grasping module that can be remotely controlled by an operation handle. By manipulating the operation handle, surgeons can conveniently reload, deliver, and release detachable coils. The distal grasping module includes a claw-like design with four pre-curved nitinol rods for clamping the coil securely during a procedure. A mechanics model based on the elliptic integral for the pre-curved beams under large deflections is proposed to model the beam behaviors and facilitate the design of the claws for adequate clamping force. Experiments were conducted to provide a quantitative suggestion on choosing the parameters of the claw and to verify the effectiveness of the elliptic integral modeling method.**

I. Introduction

Aneurysm is an outward bulging on a blood vessel which typically weakens the blood vessel wall and has rupture risk. The rupture of brain aneurysm, aortic aneurysm and cardiac aneurysm can be lethal [1].

Endovascular embolization and surgical clipping, shown in Fig.1(a and b) respectively, are typical treatments for brain aneurysms. Endovascular embolization is a minimally-invasive procedure that offers shorter hospital stay and faster post-operational recovery, compared to surgical clipping [1]. Endovascular embolization is hence more widely used for brain aneurysm treatment in recent years. Among the various embolic agents, e.g., coils, liquids, particulates, detachable plugs, and balloons [2], coil is one of the preferred types due to its simplicity to image, control and deploy. During a coiling embolization, tiny coils are delivered into the aneurysm through catheters to promote blood clotting and thus close off the aneurysm. The deployed coils prevent the aneurysm from rupturing.

Among the different types of coils, pushable coil is widely used [2], as shown in Fig. 2(a). A special guide-wire with a bulbous tip is used to push the tiny coil out of the catheter and into the targeted aneurysm. There are several limitations with the pushable coils, including coil stretching and difficulties in precise (re)positioning with potential incomplete occlusion. Therefore, detachable coils, which allow accurate coil control and ease of use, are introduced [3]. Mechanical, electrolytic, or hydrostatic coil detachment methods have been employed to release the coils when the coils arrive at the targeted location. Design of the Concerto™ system from Medtronic Inc., which employs a mechanical detachment, is shown in Fig. 2(b). Due to the existence of the detach mechanism, the coils can be precisely repositioned or even retracted before the detachment. However, the disadvantages of detachable coils include high expense (a single use instrument), potential premature coil detachment and long setup time [2].

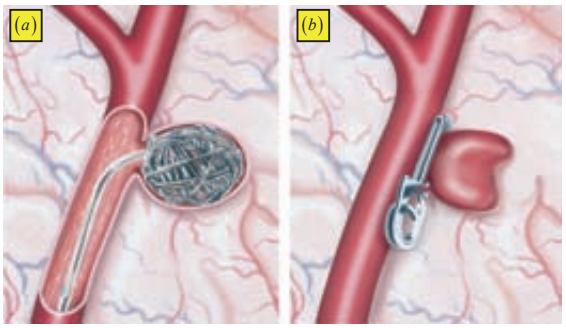

Figure 1. Aneurysm treatments: (a) endovascular coil embolization, and (b) surgical clipping [1].

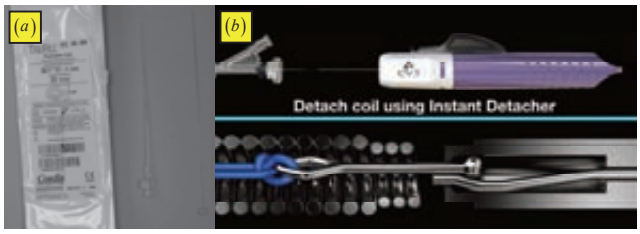

Figure 2. Endovascular coil embolization: (a) a pushable coil [2], and (b) the Concerto™ detachable coil [3].

Researchers have been working on a variety of aspects to improve endovascular coiling embolization, including: i) changing coil formation (e.g., hydrogel coils) to enhance the ability of filling the aneurysms [4, 5], ii) combining other embolization agents like balloon-assisted coil embolization (BACE) for wide-necked aneurysms [6], and iii) introducing

This work was supported in part by the National Key R&D Program of China (Grant No. 2017YFC0110800), and in part by the National Natural Science Foundation of China (Grant No. 51722507).

Chuanxiang Zhu, Yifan Wang, Yue Ding, Xiang Wang and Kai Xu are with the State Key Laboratory of Mechanical System and Vibration, School of Mechanical Engineering, Shanghai Jiao Tong University, Shanghai, 200240, China (e-mails: zcx_sjtu@sjtu.edu.cn, fan_tasy@sjtu.edu.cn, dingyue2020@sjtu.edu.cn, keith.wang@sjtu.edu.cn and k.xu@sjtu.edu.cn; corresponding author: Kai Xu).

robot-assisted embolization systems with precise and remote catheter control [7, 8].

Detachable coils can be deployed by hand with adequate precision for most of the cases. The use of detachable coils is hence on the rise [3]. Aiming at lowering the cost of detachable coils, this paper proposes a proof-of-concept design of a reloadable coil-delivery instrument. Such a reloadable design can also be potentially used together with other coil formations.

A. Design Objectives

The developed reloadable coil-delivery instrument aims at verifying the reload and release capabilities of the coil through a catheter. If the reloading and releasing of the coil can be conveniently realized, the cost of the coil-delivery instruments can be lowered. The design objectives are hence formulated as follows.

- The instrument has a distal end that can reload, hold, and release the coils.
- The instrument has a proximal end, which is operated by surgeons to reload, deliver, and release the coils.
- The distal and proximal ends of the instrument are connected such that the surgeons can remotely control the distal end to deploy coils to the targeted aneurysm via operating the proximal end.

B. Organization

The rest of this paper is structured as follows. Section II provides detailed system descriptions of the instrument and its operational process. The modeling of the large deflection of the claw-like mechanism is presented in Section III. Experimental characterizations of the instrument are detailed in Section IV, while Section V concludes the content of this paper.

II. System Descriptions

Aiming at the abovementioned objectives, a prototype of the reloadable coil-delivery instrument was designed and fabricated as shown in Fig. 3. Due to manufacturing limitations, the prototype is scaled up by 3.6 times ($\approx$ 1.5/0.42), with a ϕ1.5 mm coil compared to the ϕ0.42 mm of its commercial counterpart. The prototype consists of a grasping module as the distal end, an operation handle as the proximal end, and a micro-catheter connects the proximal and the distal ends.

The grasping module provides two features for reloading and releasing the coil. The reloading function is implemented by opening and closing a claw-like mechanism, which consists of four pre-curved nitinol rods, to grasp the coil. The releasing function is realized by pushing the coil out by a nitinol rod in the center of the micro-catheter. The two functions can be remotely controlled by a surgeon through the operation handle with one hand.

Details of the grasping module and the operation handle are presented in Section II.A and Section II.B, respectively. The whole operational process from the extracorporeal coil reloading to the intracorporeal coil releasing is presented in Section II.C.

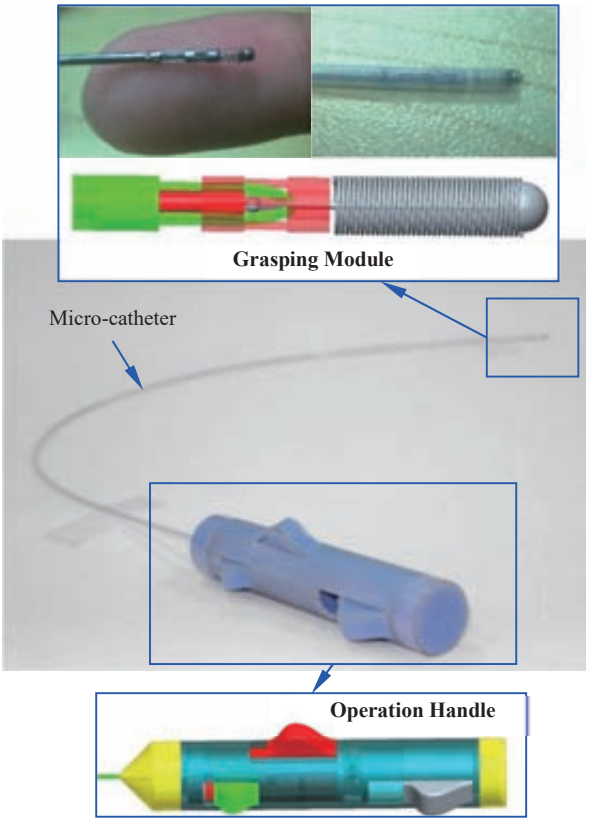

Figure 3. The 3D CAD model and the prototype of the reloadable coil-delivery instrument.

A. The Grasping Module

The entire grasping module is housed in the micro-catheter, as shown in Fig. 4. The function of the module is to reload and hold the coil conveniently and securely. Utilizing the superelasticity of nitinol, four ϕ0.2 mm nitinol rods were thermally processed to become pre-curved and were used to construct the claw.

Figure 4 shows the exploded view and the fully-assembled view of the module. As shown in Fig. 4(a), the concentric design of the micro-catheter includes, from outside to inside, a claw tube, a middle tube, and a releasing rod. The claw tube is fixed to the claws made from pre-curved nitinol rods via laser welding with the claw base. The middle tube is connected to a cage via laser welding as well. The four pre-curved rods in the claw are constrained by the cage to clamp the ball-tip tail of a coil, as shown in the assembled view in Fig. 4(b).

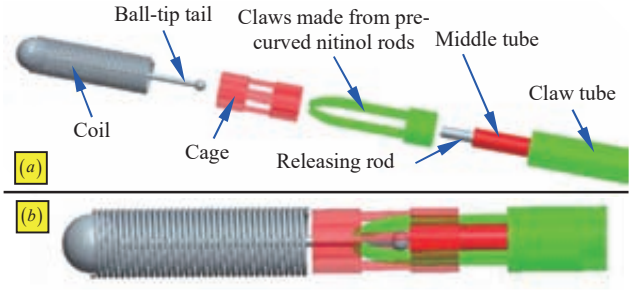

Figure 4. The grasping module: (a) the exploded view, and (b) the fully-assembled view.

When the grasping module is deployed into an aneurysm, the claw tube can retract the claw. Thus, the pre-curved nitinol rods are retracted into the holes of the cage and forced to be straight. Then the claw releases the ball-tip tail of the coil. The releasing rod then pushes the ball of the coil forward to deliver the coil into the aneurysm.

By pushing and pulling the claw tube, the middle tube, and the releasing rod, the grasping module can reload and release coils. The motion of each concentric tube or rod is independent. However, in order to securely grasp the coil and simplify the operation of surgeons, the whole grasping module should move simultaneously when the module is either moved inside the micro-catheter or pushed outside of the micro-catheter. The operation handle has been designed to meet the abovementioned requirements.

B. *The Operation Handle*

The operation handle is designed to be held and manually controlled by a surgeon for coil reloading, delivering, and releasing. It integrates three drives which can slide in the slots in the outer case. The claw tube, the middle tube, and the releasing rod are connected to corresponding drives that are denoted in Fig. 5.

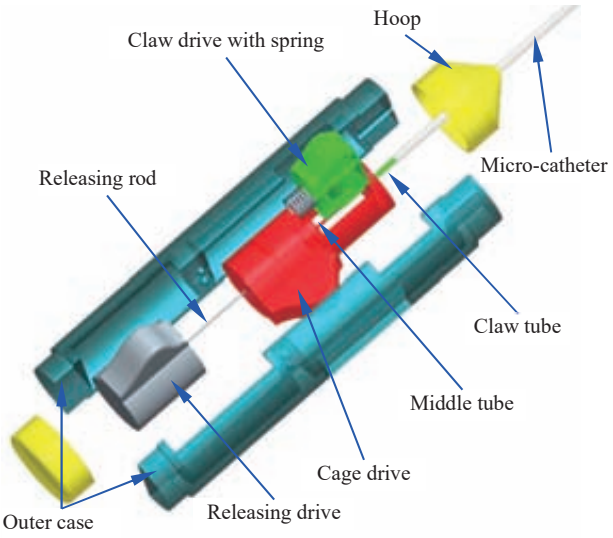

Figure 5. The operation handle.

The claw drive is embedded in the cage drive and connected to the cage drive by a spring. When a coil is grasped by the claw outside the micro-catheter, the cage and the claw should move together and remain at fixed relative positions with respect to each other. Thus, by pulling the cage drive, the coil can be pulled into the micro-catheter.

To release the coil, the cage drive can firstly be pushed. Once the cage is about to be delivered to the end of the micro-catheter, the claw drive can be moved back with respect to the cage in order to retract the claw and straighten the pre-curved nitinol rods. The desired backward movement of the claw drive is realized by designing a proper length of the sliding slot.

Once the cage drive is pushed to a desired position and the claw is fully retracted into the holes of the cage, the releasing rod can push the coil out of the catheter and complete the coil releasing process, by pushing the releasing drive. Then the ball-tip of another coil can be reloaded into the cage. The pre-curved nitinol rods of the claw can be pushed out of the corresponding holes of the cage to clamp the ball-tip tail of the reloaded coil.

C. *The Operation Procedure*

At the beginning of the operation procedure, the handle is at the initial configuration shown in Fig. 3. The releasing drive and the cage drive are at the most proximal positions in their sliding slots. The claw drive is pressed to the most distal position in the slot of the cage drive by the compression spring. The cage and the closed claw is inside the micro-catheter, and no coil is loaded. The reloading and releasing of the coils can be realized, following the procedures below.

- Reload a coil

1) A surgeon holds the operation handle and his/her thumb pushes the cage drive to the end of sliding slot. The cage is thus pushed out of the micro-catheter and the claw is opened, since its pre-curved rods are retracted into the corresponding holes of the cage. This retraction motion is generated by the relative motions of the claw drive with respect to the cage drive.

2) The surgeon inserts the ball-tip tail of a coil into the cage with another hand. By loosing the cage drive, the coil is then clamped by the claw, since the compression spring between the claw drive and the cage drive will restore to generate an equivalent motion of pushing the claw drive to extend the pre-curved nitinol rods to clamp the coil.

3) The surgeon pulls back the cage drive to pull the whole coil back into the micro-catheter and finishes the coil loading/reloading.

- Release a coil

1) The surgeon inserts the micro-catheter through the catheter that is deployed toward the targeted aneurysm.

2) The surgeon pushes the cage drive to the end of the sliding slot to open the claw and disengage the coil.

3) The surgeon pushes the releasing drive to push the whole coil out of the catheter into the aneurysm and finishes the coil releasing.

III. Modeling of the Large-Deflection Beams

The main feature of the instrument is the claw with four pre-curved beams for clamping a coil. To provide a theoretical guidance for the design of the claw, the elliptic integral is adopted for the modeling of the claw mechanism, referring to the existing studies in [9, 10]. While simulating the process of a ball-tip tail being pulled out of the claw, the deflected beam shapes can be predicted and the pull-out force can be calculated, using this model for large deflections of the nitinol rods. When a desired pull-out force is expected in the future actual-size design, the presented model can be used for guiding the design. The experimental validation in Section IV.B demonstrates the effectiveness of the derived model.

Compared to the previous results on the elliptic integral solutions in [9, 10], this paper proposes an extended elliptic integral equation by integrating the pre-curved bending radius R_i of the beam. Moreover, the force-direction parameters S_p and S_{np} are introduced to handle the different directions of the point force at the end of the beam.

Figure 6 presents a large-deflection beam with the pre-curved bending radius R_i. Considering the working condition of the claw, there is no moment exerted on the beam end. The related nomenclature is listed in Table I. The Euler-Bernoulli beam equation is presented in (1), denoting the proportional relationship between the bending moment M and the curvature $d\theta/ds$ at an arbitrary point $A(x, y)$.

$$M = EI\frac{d\theta}{ds}, \tag{1}$$

For any point $A(x, y)$ on the deflected pre-curved beam with only end force, the Euler-Bernoulli beam equation can be modified as follows.

$$M = EI\frac{d\theta}{ds} - EI\frac{1}{R_i} = S_p P(a-x) + S_{np} nP(b-y), \tag{2}$$

where EI is the flexural rigidity of the beam.

Equation (2) can be integrated to have Eq. (3) for a pre-curved beam with monotonically increasing slope.

$$\begin{cases} \alpha = \dfrac{1}{\sqrt{2}}\displaystyle\int_0^{\theta_0} \frac{1}{\sqrt{S_{np} n\cos\theta - S_p \sin\theta + \lambda}} d\theta \\ \dfrac{a}{L} = \dfrac{1}{\sqrt{2}\alpha}\displaystyle\int_0^{\theta_0} \frac{\cos\theta}{\sqrt{S_{np} n\cos\theta - S_p \sin\theta + \lambda}} d\theta \\ \dfrac{b}{L} = \dfrac{1}{\sqrt{2}\alpha}\displaystyle\int_0^{\theta_0} \frac{\sin\theta}{\sqrt{S_{np} n\cos\theta - S_p \sin\theta + \lambda}} d\theta \end{cases}, \tag{3}$$

where $\alpha = \sqrt{PL^2/EI}$ and $\lambda = S_p \sin\theta_0 - S_{np} n\cos\theta_0 + EI/2PR_i^2$.

As equation (3) cannot be solved directly, the elliptic integral functions introduced in [11] are used to transform Eq. (3) into closed-form expressions. The elliptic integral functions are presented as follows.

$$\begin{cases} F(\gamma, t) = \displaystyle\int_0^{\gamma} \frac{1}{\sqrt{1 - t^2 \sin^2\delta}} d\delta \\ E(\gamma, t) = \displaystyle\int_0^{\gamma} \sqrt{1 - t^2 \sin^2\delta}\, d\delta \end{cases}, \tag{4}$$

where t denotes the modulus with $t \in (0,1)$, and γ denotes the amplitude.

The elliptic integral solution to Eq. (3) is divided into two cases of $|\lambda| > \eta$ and $|\lambda| \le \eta$, since the modulus in the elliptic integral functions should conform to $t \in (0,1)$.

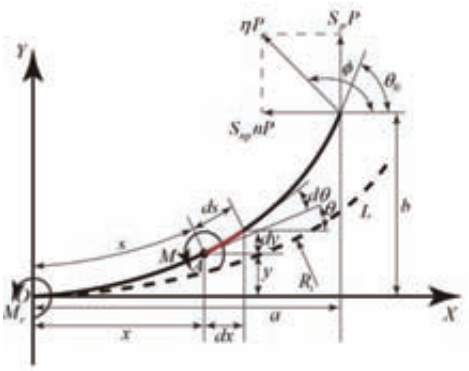

Figure 6. Large deflection of a pre-curved cantilever beam (original shape denoted by the dashed line).

TABLE I. NOMENCLATURE FOR THE ELLIPTIC INTEGRAL SOLUTION

Symbol	Description
L	Total length of the beam
x	Horizontal displacement of a point on the deflected beam
y	Vertical displacement of a point on the deflected beam
s	Length of a point along the beam
$\theta(s)$	Slope of a point on the deflected beam
θ_0	Slope of the beam end
$R_i(s)$	Radius of the pre-curved beam
$M(s)$	Resultant moment of a point on the deflected beam. The positive direction is counterclockwise.
M_r	Resultant moment at the base point on the deflected beam.
a	Horizontal displacement of the beam end.
b	Vertical displacement of the beam end.
P	Scalar vertical component of the resultant force exerted on the beam end.
nP	Scalar horizontal component of the resultant force exerted on the beam end, where n is a scalar parameter.
ηP	Resultant force exerted on the beam end, with $\eta = \sqrt{1+n^2}$.
S_p	Direction coefficient of the vertical resultant force component. The positive direction is shown in Fig. 6. S_pP is the vertical resultant force component exerted on the beam end.
S_{np}	Direction coefficient of the horizontal resultant force component. The positive direction is shown in Fig. 6. $S_{np}nP$ is the horizontal resultant force component exerted on the beam end.

A. Case $|\lambda| \le \eta$

With the Jacobian elliptic functions introduced in [11], the following relations are firstly derived as follows.

$$\begin{cases} \sin^2\gamma = (\eta + S_p \sin\theta - S_{np} n\cos\theta)/(\lambda + \eta) \\ \cos^2\gamma = 1 - \sin^2\gamma = (\lambda - S_p \sin\theta + S_{np} n\cos\theta)/(\lambda + \eta) \\ \Delta\gamma = 1 - t^2 \sin^2\gamma = (\eta - S_p \sin\theta + S_{np} n\cos\theta)/2\eta \end{cases}, \tag{5}$$

where $t = \sqrt{(\lambda+\eta)/2\eta} \in (0,1)$.

With the above relations and trivial deductions, the final elliptic integral solution for the pre-curved large-deflection beams in the case of $|\lambda| \le \eta$ is derived as follows.

$$\begin{cases} \alpha = S_p f \big/ \sqrt{\eta} \\ \dfrac{a}{L} = S_p \left(\sqrt{2}\sqrt{\eta} c - S_{np} n \eta f + 2 S_{np} n \eta e \right) \Big/ \eta^{\frac{5}{2}} \alpha \\ \dfrac{b}{L} = \left(S_{np} n \sqrt{2} \sqrt{\eta} c + \eta f - 2 \eta e \right) \Big/ \eta^{\frac{5}{2}} \alpha \end{cases}, \quad (6)$$

where $\begin{cases} c = \sqrt{\lambda + S_{np} n} - \sqrt{\lambda - S_p \sin\theta_0 + S_{np} n \cos\theta_0} \\ f = F(\gamma_2, t) - F(\gamma_1, t) \\ e = E(\gamma_2, t) - E(\gamma_1, t) \\ \gamma_1 = \arcsin \sqrt{(\eta - S_{np} n)/(\lambda + \eta)} \\ \gamma_2 = \arcsin \sqrt{(\eta + S_p \sin\theta_0 - S_{np} n \cos\theta_0)/(\lambda + \eta)} \end{cases}$.

The sign of $d\theta$ changes according to the inflection point(s) on the deflected beams. However, in this study there is no inflection point on the beam, since no moment is applied on the beam end. Thus, the elliptic integral solution for beams with inflection point(s) will not be involved.

B. Case $|\lambda| > \eta$

With the Jacobian elliptic functions introduced in [11], the second case has the following relations.

$$\begin{cases} \sin^2\gamma = (\eta + S_p \sin\theta - S_{np} n \cos\theta)/2\eta \\ \cos^2\gamma = 1 - \sin^2\gamma = (\eta - S_p \sin\theta + S_{np} n \cos\theta)/2\eta \\ \Delta\gamma = 1 - t^2 \sin^2\gamma = (\lambda - S_p \sin\theta + S_{np} n \cos\theta)/(\lambda + \eta) \end{cases}, \quad (7)$$

where $t = \sqrt{2\eta/(\lambda + \eta)} \in (0,1)$.

With the relations above, the final elliptic integral solution for the pre-curved large-deflection beams in the case of $|\lambda| > \eta$ is derived as follows.

$$\begin{cases} \alpha = \dfrac{\sqrt{2} S_p}{\sqrt{\lambda + \eta}} f \\ \dfrac{a}{L} = \dfrac{\sqrt{2}\left(S_p \sqrt{\lambda + \eta} c - S_{np} n \lambda f + S_{np} n (\lambda + \eta) e \right)}{\eta^2 \alpha \sqrt{\lambda + \eta}} \\ \dfrac{b}{L} = \dfrac{\sqrt{2}\left(S_p S_{np} n \sqrt{\lambda + \eta} c + \lambda f - (\lambda + \eta) e \right)}{\eta^2 \alpha \sqrt{\lambda + \eta}} \end{cases}, \quad (8)$$

where $\begin{cases} c = \sqrt{\lambda + S_{np} n} - \sqrt{\lambda - S_p \sin\theta_0 + S_{np} n \cos\theta_0} \\ f = F(\gamma_2, t) - F(\gamma_1, t) \\ e = E(\gamma_2, t) - E(\gamma_1, t) \\ \gamma_1 = \arcsin \sqrt{(\eta - S_{np} n)/2\eta} \\ \gamma_2 = \arcsin \sqrt{(\eta + S_p \sin\theta_0 - S_{np} n \cos\theta_0)/2\eta} \end{cases}$.

IV. Experimental Characterizations

A scaled prototype was fabricated as shown in Fig. 3. Several experiments were conducted to first verify the working principle of the instrument. By manipulating the operation handle, the functions of reloading, delivering, and releasing of the detachable coils were accomplished, suggesting the effectiveness of the reloadable coil-delivery instrument.

Another set of experiments were then conducted to obtain representative results on the pull-out forces of the claws with different bending curvatures. The shapes and pull-out forces of the claws were also calculated by the elliptic integral solutions. The effectiveness of the modeling approach was verified by comparing the experimental and calculated results.

A. Clamping Force Experiments

In this set of experiments, several ϕ0.2 mm nitinol rods were adopted as the beams of the claws. The rods have been thermally processed to have different bending radii. Ideally, the higher the rod's curvature is, the greater pull-out force the claw can reach.

To experimentally investigate the pull-out force, three representative initial strains (3%, 5%, and 7%) for the pre-curved beams within the maximal allowed strain (10%) of the nitinol rod were used. The radii of the pre-curved beams under different initial strains are shown in Fig. 7. Three claws made from beams with three different initial strains were prepared. A ϕ0.6mm ball is used as the detachable coil, which serves as the eyelet of the Concerto™ detachable coils [3].

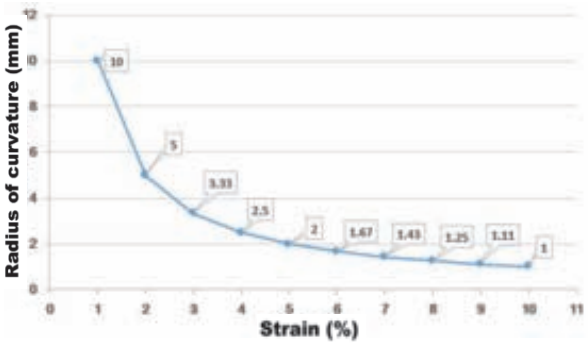

Figure 7. The relationships between the pre-curved radii and the initial strains of ⌀0.2 mm nitinol rod.

The experimental setup is shown in Fig. 8. The ball is attached to a force sensor (ATI Nano 17 F/T Sensor) which records the pull-out force. Micrometer-1 is used to pull the claw away from the ball. A servo motor (Maxon DC-Max 22S with gearbox and encoder) rotates the micrometer-1 with a constant velocity in each measurement. Micrometer-2 is used to control the stretched-out length of the four nitinol rods, since claws with different pre-curved radius requires different lengths to clamp the ball.

During each measurement, the ball was pulled out of the claw and the pull-out force was recorded. The raw data were properly filtered, and the pull-out force of claws with different initial strains are plotted in Fig. 9. Each measurement started from pushing the ball back to the center

of the claw, thus each curve starts with few seconds of negative force. Then the ball was slowly pulled out by the micrometer-1 and the force turned positive. With the ball being pulled out of the claw, the pull-out force first rose and then dropped as the ball escaped from the claw.

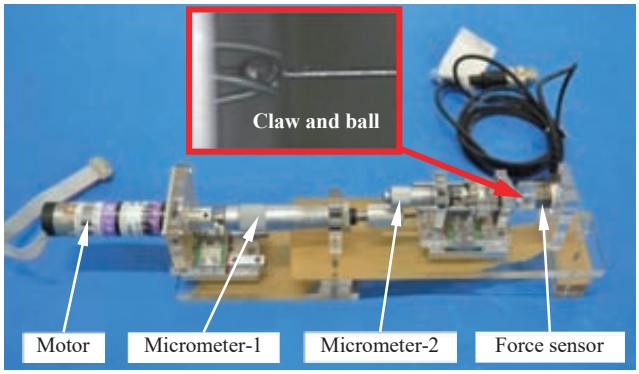

Figure 8. The experiental setup for measuring the pull-out force.

Ideally the claw with 7% initial strain should produce the largest pull-out force among the three claws. However, the recorded data of the claw with 5% initial strain shows the highest pull-out force of about 0.76 N, in comparison with 0.63 N by the claw with 7% initial strain. One possible reason is the limited accuracy of the manual fabrication of the claws. The difference of radius between the 5% and 7% strain rods is only 0.57 mm as shown in Fig. 7, which may have smaller influence on the pull-out force, compared to the uncertainty of the manual fabrication.

As shown in the snapshots in Fig. 9, during the pull-out, the ball was not evenly resisted by the four pre-curved rods. One of the beams, which opposites the other three beams that were assembled more closely, deflected more when the ball was pulled out. This is mainly due to the limited accuracy of the manual fabrication such that the four beams were not perfectly symmetric. In addition, during the pull-out test, the ball and the claw were not perfectly aligned. Therefore, the recorded pull-out force should be considered as the resistance force mainly produced by only one pre-curved beam of the claw.

B. Verification of the Elliptic Integral Modeling

Using the elliptic integral modeling method presented in Section III, the pull-out forces of different claws were calculated and the beam shapes were obtained. The effectiveness of the modeling was verified by the pull-out force measurements from Section IV.A.

Using the MATLAB built-in function 'fsolve', equations (6) and (8) can be solved with proper initial guess of n and P. Other known parameters are listed in Table II.

During the process of the coil detachment, the bending shapes of the claw beam were obtained by the elliptic integral model. The calculated deflected beam shapes, denoted by green curves in Fig. 10, conform well to the camera-captured deflected beam shapes. At the moment shown in Fig. 10(a), the calculated pull-out force for the claw with 5% initial strain is 0.60 N, which is smaller than the recorded pull-out force 0.76 N. In Fig. 10(b), the calculated and experimentally measured pull-out force for claw with 7% initial strain is 0.49 N and 0.62 N, respectively. The discrepancy between the calculated and the measured force is possibly due to the limited manufacture accuracy, including the micro manufacturing limitation on welding the small ball to the coil and the asymmetric deflections of the four pre-curved rods.

The pre-curved beam at its original shape is denoted by the red curve. A series of deflected beam shapes during pulling out experiment were obtained by the elliptic integral modeling method and are denoted by blue curves in Fig. 10. The shapes obtained by the elliptic integral model conformed well to the captured beam shapes in the experiments, suggesting the effectiveness of the elliptic integral modeling method proposed in this paper.

TABLE II. PARAMETERS FOR THE ELLIPTIC INTEGRAL MODEL

Symbol	Description
r	Cross-section radius of the claw beams. $r = 0.1$ *mm*.
$R_i = \frac{r}{\varepsilon}$	Bend radius of the pre-curved undeflected beam. ε is the initial strain of the pre-curved nitinol rod which is 3%, 5%, or 7%.
$E = 32.1$ *GPa*	Young's modulus of nitinol rod. Acquired by Zwick Roell material testing machine according to ISO 6892:1998.
$S_p = -1$	Direction of the vertical component of the end force.
$S_{np} = -1$	Direction of the horizontal component of the end force
a	Horizontal displacement of the beam end extracted by high resolution photo of the deflected nitinol rod.
b	Vertical displacement of the beam end extracted by high resolution photo of the deflected nitinol rod.
θ_0	Slope of the beam end extracted by high resolution photo of the deflected nitinol rod.
L	L = 1.5 mm and 1.2 mm for beam with 5% and 7% initial strain, respectively.

V. CONCLUSIONS AND FUTURE WORK

This paper presents the development and experimental characterizations of a reloadable coil-delivery instrument for detachable coils for embolization treatment of aneurysms. The reloadable coil-delivery instrument consists of the grasping module and the operation handle. Four pre-curved nitinol rods compose the claw which can clamp an embolization coil. The operation handle with three drives can be manipulated by a surgeon for reloading, delivery and releasing of the coils. The pull-out force measurements give a preliminary suggestion on choosing the specification of the claw. The verification experiments on the elliptic integral model show the effectiveness of this modeling method. The proposed large deflection modeling method can facilitate the design process of the claws for desired clamping forces.

Future efforts will be primarily focused on i) fabricating the prototype with the same scale as the commercial product, and ii) numerically optimization of the parameters of the claw (e.g., the pre-curved radius and the diameter of rods) based on the proposed elliptic integral modeling approach.

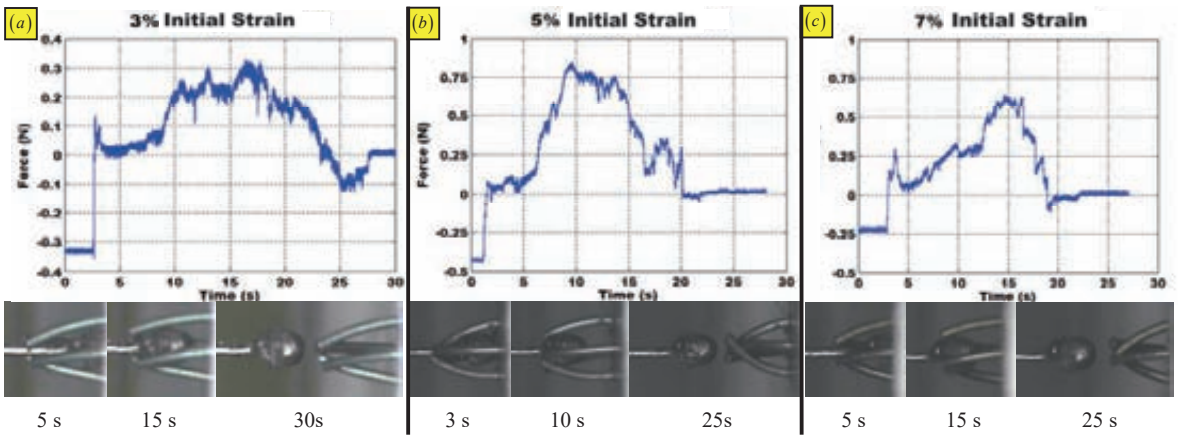

Figure 9. The measured pull-out forces of the claws with different initial strains: (a) 3% initial strain, (b) 5% initial strain, and (c) 7% initial strain.

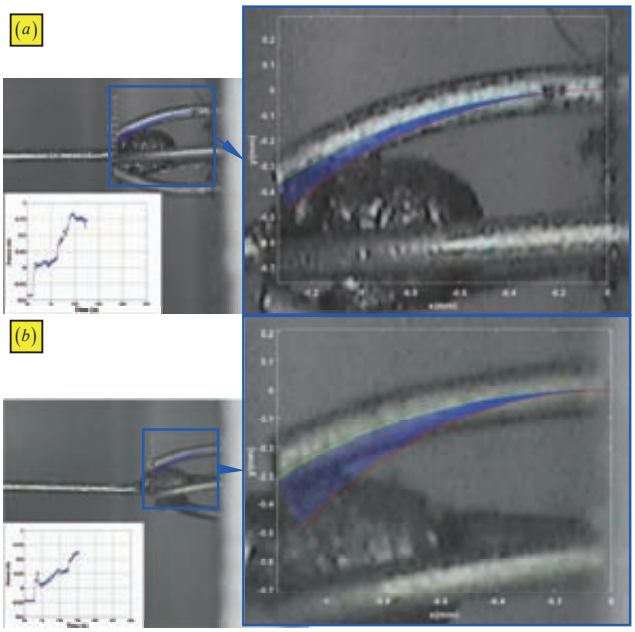

Figure 10. The verification of the elliptic integral solution on the pre-curved-beam deflection: (a) the verification of claw with 5% initial strain, and (b) 7% initial strain. On the enlarged insets, the green curves denote the matching results between the calculated and the camera-captured beam shapes. The red curves denote the original pre-curved shape of the beams before the pull-out of the ball. The blue curves denote two series of calculated beam shapes during the pull-out.

REFERENCES

[1] S. C. Johnston, C. B. Wilson, V. V. Halbach, R. T. Higashida, C. F. Dowd, M. W. McDermott, C. B. Applebury, T. L. Farley, and D. R. Gress, "Endovascular and Surgical Treatment of Unruptured Cerebral Aneurysms: Comparison of Risks," *Annals of Neurology,* vol. 48, No.1, pp. 11-19, 2000.

[2] S. Vaidya, K. R. Tozer, and J. Chen, "An Overview of Embolic Agents," in *Seminars in Interventional Radiology*, 2008, pp. 204-215.

[3] R. T. Gandhi and R. Malik, "Clinical Versatility of the Concerto™ Detachable Coils in Peripheral Embolization," *Endovascular Today,* vol. 2014, No.September, pp. 32-36, September 2014.

[4] D. F. Kallmes and N. H. Fujiwara, "New Expandable Hydrogel-Platinum Coil Hybrid Device for Aneurysm Embolization," *American Journal of Neuroradiology,* vol. 23, No.9, pp. 1580-1588, Oct 2002.

[5] H. J. Cloft, "HydroCoil for Endovascular Aneurysm Occlusion (HEAL) Study: Periprocedural Results," *American Journal of Neuroradiology,* vol. 27, No.2, pp. 289-292, Feb 2006.

[6] M. Sluzewski, W. J. Van Rooij, G. N. Beute, and P. C. Nijssen, "Balloon-Assisted Coil Embolization of Intracranial Aneurysms: Incidence, Complications, and Angiography Results," *Journal of Neurosurgery,* vol. 105, No.3, pp. 396-399, Sep 2006.

[7] T. Carrell, N. Dastur, R. Salter, and P. Taylor, "Use of a Remotely Steerable "Robotic" Catheter in a Branched Endovascular Aortic Graft," *Journal of Vascular Surgery,* vol. 55, No.1, pp. 223-225, 2012.

[8] T. Lu, S. Owji, P. Chinnadurai, T. M. Loh, A. Schwein, A. B. Lumsden, and J. Bismuth, "Robotic-Assisted Coil Embolization of Ascending Aortic Pseudoaneurysm," *Annals of Thoracic Surgery,* vol. 102, No.5, pp. e451-e453, Nov 2016.

[9] K. Xu and N. Simaan, "Analytic Formulation for the Kinematics, Statics and Shape Restoration of Multibackbone Continuum Robots via Elliptic Integrals," *Journal of Mechanisms and Robotics,* vol. 2, No.011006, pp. 1-13, Feb 2010.

[10] A. Zhang and G. Chen, "A Comprehensive Elliptic Integral Solution to the Large Deflection Problems of Thin Beams in Compliant Mechanisms," *Journal of Mechanisms and Robotics,* vol. 5, No.2, p. 021006, Mar 2013.

[11] P. F. Byrd and M. D. Friedman, *Handbook of Elliptic Integrals for Engineers and Scientists*, Second Edition, Revised ed. New York: Springer-Verlag, 1971.